

The Hot Circum-Galactic Medium in the eROSITA All Sky Survey

II. Scaling Relations between X-ray Luminosity and Galaxies' Mass

Yi Zhang^{1,*}, Johan Comparat¹, Gabriele Ponti^{2,1}, Andrea Merloni¹, Kirpal Nandra¹, Frank Haberl¹, Nhut Truong^{3,4},
Annalisa Pillepich⁵, Nicola Locatelli², Xiaoyuan Zhang¹, Jeremy Sanders¹, Xueying Zheng¹, Ang Liu¹, Paola
Popesso⁶, Teng Liu^{7,8}, Peter Predehl¹, and Mara Salvato¹

¹ Max-Planck-Institut für extraterrestrische Physik (MPE), Gießenbachstraße 1, D-85748 Garching bei München, Germany

² INAF-Osservatorio Astronomico di Brera, Via E. Bianchi 46, I-23807 Merate (LC), Italy

³ NASA Goddard Space Flight Center, Greenbelt, MD 20771, USA

⁴ Center for Space Sciences and Technology, University of Maryland, 1000 Hilltop Circle, Baltimore, MD 21250, USA

⁵ Max-Planck-Institut für Astronomie, Königstuhl 17, 69117 Heidelberg, Germany

⁶ European Southern Observatory, Karl Schwarzschildstrasse 2, D-85748 Garching bei München, Germany

⁷ Department of Astronomy, University of Science and Technology of China, Hefei 230026, China

⁸ School of Astronomy and Space Science, University of Science and Technology of China, Hefei 230026, China

Received ; accepted

ABSTRACT

Aims. Understanding how the hot circum-galactic medium (CGM) properties relate to the galaxy's properties can constrain galaxy evolution models. We aim to measure the scaling relations between the X-ray luminosity of the hot CGM and the fundamental properties of a galaxy, i.e., its stellar mass and halo mass.

Methods. We calculate the X-ray luminosity of the hot CGM based on the surface brightness profiles of central galaxy samples measured in Zhang et al. (2024a, submitted) from Spectrum Roentgen Gamma (SRG)/eROSITA all-sky survey data. We relate the X-ray luminosity to the galaxies' stellar and halo mass. We compare the observed relations to the TNG, EAGLE, and SIMBA simulations.

Results. The hot CGM X-ray luminosity correlates with the galaxy's stellar mass (M_*). It increases from $2.1 \pm 1.3 \times 10^{39}$ erg/s to $2.0 \pm 0.1 \times 10^{41}$ erg/s, when $\log(M_*)$ increases from 10.0 to 11.5. A double power law describes the correlation, with a break at $\log(M_*) = 11.28 \pm 0.03$ and a power-law index of 1.9 ± 0.2 (4.2 ± 0.1) below (above) the break. The hot CGM X-ray luminosity as a function of halo mass is measured within $\log(M_{500c}) = 11.3 - 13.7$, extending our knowledge of the scaling relation by more than two orders of magnitude. $L_{X,CGM}$ increases with M_{500c} from $2.7 \pm 0.9 \times 10^{39}$ erg/s at $\log(M_{500c}) = 11.3$ to $9.2 \pm 0.4 \times 10^{41}$ erg/s at $\log(M_{500c}) = 13.7$. The relation follows a power law of $\log(L_{X,CGM}) = (1.35 \pm 0.04) \times \log(M_{500c}) + (23.8 \pm 0.5)$. We find a general agreement between simulations and observation.

Conclusions. We explore, at the low mass end, the average scaling relations between the CGM X-ray luminosity and the galaxy's stellar mass or halo mass, which constitutes a new benchmark for galaxy evolution models and feedback processes.

Key words. X-ray, galaxies, circum-galactic medium

1. Introduction

In the paradigm of hierarchical structure formation driven by gravitation, the primordial density field made of dark matter and baryons undergoes collapse to form virialized objects: halos and galaxies (White & Rees 1978). Galaxies, halos, and their environments co-evolve, and their properties are correlated (Muldrew et al. 2012). For example, Leauthaud et al. (2012a,b) and Coupon et al. (2015) observed a tight relation between the stellar mass (M_*) of a galaxy and its host dark matter halo mass (M_{halo}). Moreover, galaxies follow a well-known main sequence between star formation rate and stellar mass (Whitaker et al. 2012; Iyer et al. 2018), and show a correlation between their size and stellar mass (Mowla et al. 2019a,b). In this article, we investigate the relation between the total X-ray luminosity of a halo and the stellar or halo mass.

In the local Universe, for the early-type galaxies (ETGs), the relation between L_X and M_* , dynamical mass (baryon plus dark

matter), central optical profile of galaxy, and temperature of gas (T_X) within < 50 Mpc has been studied (Kim & Fabbiano 2013, 2015; Goulding et al. 2016; Forbes et al. 2017). The relations measured support the necessity of AGN feedback in massive ETGs and demands of stellar feedback in less massive ETGs (Choi et al. 2015). For the late-type galaxies (LTGs), the Chandra survey of nearby (< 30 Mpc) highly inclined disc galaxies found correlations between L_X and SFR, supernova (SN) mechanical energy input rate and T_X , which implies a stellar feedback origin of the X-ray emission (Li & Wang 2013; Wang et al. 2016). A weaker correlation between L_X and M_* is found in disk galaxies, especially star-burst galaxies, compared to ETGs.

To characterize such relations at higher redshift, one needs to resort to stacking techniques to overcome the intrinsic dim X-ray emission of the CGM. By stacking 250,000 galaxies selected from SDSS with the ROSAT ALL-Sky survey data, Anderson et al. (2015) found the $L_X - M_*$ relation to be steeper than expected from self-similar model predicted above $\log(M_*) > 11.0$, implying the existence of non-gravitational heating. For the same galaxy sample, a general correlation between the galaxy stel-

* yizhang@mpe.mpg.de

lar mass and the Comptonization Y -parameter was measured by (Planck Collaboration et al. 2013). With an improved spatial resolution, the Y -Mass relation is measured at the high mass end (Schaan et al. 2021; Pandey et al. 2022). More recently, Das et al. (2023) have extended the relation down to $M_* > 5 \times 10^{10} M_\odot$ by cross-correlating the WISE and SuperCOSMOS photometric redshift galaxy sample (Bilicki et al. 2016) with ACT and Planck. They found a steeper Y -Mass relation than the self-similar model predicted.

The extended ROentgen survey with an Imaging Telescope Array (eROSITA) on board the Spektrum Roentgen Gamma (SRG) orbital observatory provides the new X-ray data for stacking experiments. Recently, with eROSITA and its PV/eFEDS observations covering 140 square degrees, Comparat et al. (2022) stacked $\sim 16,000$ central star-forming and quiescent galaxies selected from the GAMA spectroscopic galaxy survey; later, Chadayammuri et al. (2022) stacked $\sim 1,600$ massive star-forming and quiescent galaxies selected from SDSS in the same eFEDS field. The difference in the sample selection led to different interpretations of the results (we will discuss in detail in Zhang et al. 2024c, in preparation).

In this work, we use the state-of-the-art stacking results obtained in the companion paper Zhang et al. 2024a (submitted, hereafter Paper I). There, we use the first four of the planned eight all-sky surveys (eROSITA all-sky survey, eRASS:4) (Merloni et al. 2012; Predehl et al. 2021; Sunyaev et al. 2021; Merloni et al. 2024) and galaxy samples with high completeness (Dey et al. 2019; Zou et al. 2019; Tinker 2021, 2022) to measure the average surface brightness profiles of the CGM, after modeling and subtracting the contaminating X-ray emission from AGN, X-ray Binaries (XRB) and satellite galaxies.

In the literature, the gas within the virial radius is generally called CGM for isolated L^* galaxies and is called intragroup medium (IGrM) or intracluster medium (ICM) for more massive systems. However, the separation between them is hard to define physically (and observationally) and is not the goal of this work. For simplicity, we define CGM as the gas within the radius R_{500c}^1 of the central galaxy, regardless of the halo mass. We integrate the X-ray surface brightness profiles in Paper I to calculate the X-ray luminosity. We study the relations between the X-ray luminosities and galaxies' stellar or halo masses.

The eROSITA X-ray data reduction, stacking method, and galaxy samples are detailed in Paper I. This paper is organized as follows. The relevant and additional methods are explained in Sect. 2. The relations obtained between X-ray luminosity and masses of galaxies are presented in Sect. 3. The implication of the observed scaling relations is discussed in Sect. 4. We use Planck Collaboration et al. (2020) cosmological parameters: $H_0 = 67.74$ km/s/Mpc and $\Omega_m = 0.3089$. The log in this work designates \log_{10} .

In two additional companion papers also based on the measurements from Zhang et al. (2024a), we investigate (i) the trends as a function of specific star formation rate (Zhang et al. 2024c, in preparation) and (ii) the possible dependence on azimuth angle (Zhang et al. 2024d, in preparation).

2. Methods

2.1. X-ray luminosity

The total X-ray luminosity L_{X,r_1} around a galaxy is calculated by integrating the (background subtracted) surface brightness pro-

¹ R_{500c} is the radius where the density is 500 times the critical density of the local universe. The halo mass within R_{500c} is denoted as M_{500c} .

files $S_{X,gal} - S_{X,bg}$ up to a given radius r_1 ,

$$L_{X,r_1} = \int_0^{r_1} (S_{X,gal} - S_{X,bg}) \times A_{shell} [erg/s], \quad (1)$$

where $S_{X,gal}$ is the observed X-ray surface brightness of stacked galaxy, $S_{X,bg}$ is the background X-ray surface brightness, A_{shell} is the area size of integrated annulus.

The uncertainty on L_{X,r_1} is estimated from the quadratic sum of the Poisson error and uncertainty estimated with Jackknife resampling (Andrae 2010; McIntosh 2016, Paper I). We find that the Poisson error is negligible, benefiting from the large galaxy sample. The main Jackknife uncertainty reflects the scatter of the X-ray luminosities of the stacked galaxy population².

The luminosity is calculated in the energy bin $0.5 - 2$ keV (in the rest frame). We integrate the X-ray emission within R_{500c} , and the obtained luminosity is denoted as $L_{X,total}$.

Without masking detected X-ray sources, $L_{X,total}$ is the total X-ray luminosity of all sources within R_{500c} , including the point sources, i.e. AGNs and XRBs, and extended CGM. After masking detected X-ray sources, we integrate the X-ray emission within R_{500c} and obtain $L_{X,mask}$. We follow the methods detailed in Paper I: we subtract the X-ray emission from unresolved AGN and XRB that reside in the stacked galaxies and the satellite galaxies ($L_{X,AGN+XRB+SAT}$), to obtain the X-ray luminosity of the residual emission which is assumed to come from only the hot CGM within R_{500c} : $L_{X,CGM}$.

2.2. Galaxy samples

The galaxy sample selection method is detailed in Paper I. The galaxy samples are built to achieve a high completeness within a maximum redshift. We use three samples defined as:

- (i) *CEN sample*: the central galaxy sample selected from the SDSS Main Galaxy Sample (MGS, spectroscopic redshift) binned in stellar mass (derived from spectral energy distribution fitting) (Strauss et al. 2002; Tinker 2021, 2022). The sample includes 85,222 galaxies in the stellar mass range $10.0 < \log(M_*) < 11.5$ and spectroscopic redshift $0.01 < z_{spec} < 0.19$. The central galaxies are identified by the halo-based group finder mechanism, with a misclassified probability of less than 1% (Tinker 2021).
- (ii) *CEN_{halo} sample*: the central galaxy sample, defined above, is now binned in halo mass. The halo mass (M_{500c}^3) is estimated by the halo-based group finder algorithm (Tinker 2021).
- (iii) *Isolated sample*: the isolated galaxy sample is selected from the DESI legacy survey DR9 galaxy catalog binned in stellar mass (LS DR9, photometric) (Dey et al. 2019; Zou et al. 2019). The sample includes 213,514 galaxies in the stellar mass range $9.5 < \log(M_*) < 11.5$ and photometric redshift $0.01 < z_{phot} < 0.4$. The isolated galaxies are selected to minimize the satellite boost effect, as described in Paper I. By virtue of their selection, the isolated galaxies are sub-samples of the central galaxies living in under-dense environments.

² The X-ray luminosity scatter of the stacked galaxy population is larger when the detected X-ray sources are not masked during the stacking.

³ The halo mass provided in the catalog Tinker (2021) is M_{200m} , the mass within the radius where the mean interior density is 200 times the background universe density. To make the comparison to literature easier, we convert the M_{200m} to M_{500c} with the mass-concentration relation model from Ishiyama et al. (2021).

2.3. Simulation datasets and computation of the intrinsic X-ray emission

To facilitate the interpretation of our observational results, we utilize publicly available simulated datasets from the three distinguished cosmological hydrodynamical simulations: TNG100 from IllustrisTNG (Marinacci et al. 2018; Naiman et al. 2018; Springel et al. 2018; Pillepich et al. 2018; Nelson et al. 2019b,a), EAGLE (Crain et al. 2015; Schaller et al. 2015; Schaye et al. 2015; McAlpine et al. 2016), and SIMBA (Davé et al. 2019)⁴. These simulations aim to model galaxy formation and evolution within a Λ CDM universe with consistent cosmological parameters and simulated box (~ 100 kpc per size). The three models, while implementing various astrophysical processes relevant to galaxy formation, differ from each other in terms of modeling feedback from stellar and supermassive black hole activities. These variations on feedback modeling could result in significantly different predictions on the CGM properties (Truong et al. 2023).

We compare simulated galaxies with stellar mass $M_* > 10^{9.5} M_\odot$ to the stacking results. For each simulated galaxy, the X-ray luminosity of the CGM is measured in the 0.5 – 2 keV range and within a radial range of $(0.15 - 1) R_{500c}$, following the methods detailed in Truong et al. (2021); Comparat et al. (2022). In short, the X-ray luminosity is derived from the thermodynamic properties of gas particles (non-star-forming) by employing a single-temperature APEC model (Smith et al. 2001). Note that the computed X-ray emissions of the CGM are intrinsic and do not account for any observational effects.

2.4. Scaling relation models

We parametrize the single power law as

$$\log(L_{X,\text{CGM}}) = L_0 + \alpha \log(M). \quad (2)$$

The single power law has two parameters L_0 and the slope α . We parametrize the broken power law as

$$\log(L_{X,\text{CGM}}) = L_0 + \alpha_1 \log\left(\frac{M}{M_0}\right) + \delta(\alpha_2 - \alpha_1) \log\left(\frac{1}{2} \left(1 + \frac{M}{M_0}\right)^{1/\delta}\right), \quad (3)$$

with a break at M_0 , a slope of α_1 for $M_* < M_0$ and another slope α_2 for $M_* > M_0$, δ controls how broad the transition between the two slopes is.

We use the maximum likelihood method and the Markov chain Monte Carlo (MCMC) chains to estimate the best-fit parameters and their 1σ uncertainties (Paper I, Hogg et al. 2010).

3. Results

This section presents the scaling relations we obtain between the X-ray luminosity and M_* or M_{500c} . The relationship between $L_{X,\text{total}}$ and M_* of galaxies (without masking X-ray sources) is presented in Sect. 3.1. The inferred $L_{X,\text{CGM}}$ to M_* relation compared to the simulations is presented in Sect. 3.2. The relationships between $L_{X,\text{total}}$ or $L_{X,\text{CGM}}$ and M_{500c} of galaxies with comparison to simulations are presented in Sect. 3.3.

⁴ We note that here we use versions of EAGLE and SIMBA that are reprocessed to share the same data format with TNG simulation (Nelson et al. 2019b). The reprocessing ensures that simulated structures, e.g., galaxies and their host halos, as well as their properties, are identified in the same manner among the three simulations. This also allows the usage of identical analysis methods.

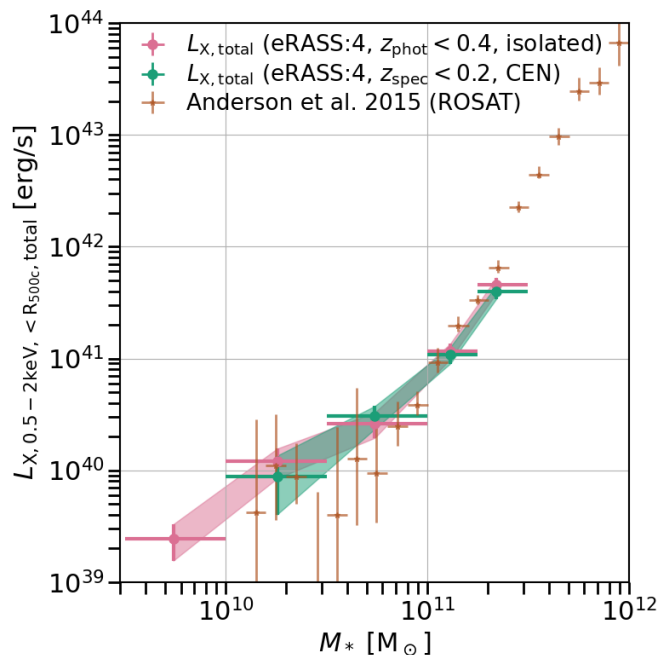


Fig. 1: The total 0.5 – 2 keV X-ray luminosity ($L_{X,\text{total}}$) within R_{500c} of galaxies as a function of stellar mass M_* , for isolated galaxies (red) and central galaxies (green). The measurement from Anderson et al. (2015) is plotted in brown.

3.1. $L_{X,\text{total}} - M_*$ relation

Based on the central and isolated galaxies stacking, the $L_{X,\text{total}} - M_*$ relation is plotted in Fig. 1. Note that $L_{X,\text{total}}$ includes the emission from AGN, XRB, and hot gas. $L_{X,\text{total}}$ increases from $2.4 \pm 0.9 \times 10^{39}$ erg/s to $4.6 \pm 0.7 \times 10^{41}$ erg/s, when M_* increases from $3 \times 10^9 M_\odot$ to $3 \times 10^{11} M_\odot$ (see Table 1). The increase of $\log(L_{X,\text{total}})$ with $\log(M_*)$ appears non-linear: below $\log(M_*) \approx 11.0$ the increase is slower, and it then gets faster with $\log(M_*)$. The $L_{X,\text{total}} - M_*$ relations by stacking the isolated and CEN sample give consistent results, with a difference of less than 1σ . Notice that the isolated and CEN samples have a maximum redshift difference of 0.2, i.e. about a 2 Gyr age difference. We do not detect redshift evolution of the $L_{X,\text{total}} - M_*$ relation within the limited redshift range.

In Fig. 1, we also compare the obtained $L_{X,\text{total}} - M_*$ relation to Anderson et al. (2015, Fig. 5, top panel). They measured the X-ray luminosity of the ‘locally brightest galaxies’ (similar to the CEN sample) using ROSAT. The $L_X - M_*$ relations in the two works agree with a difference less than 1σ . Thanks to eRASS:4, significant progress is made: we narrow down the uncertainties on the relation by a factor of about ten at $\log(M_*) = 10.7$ and by a factor of about two at $\log(M_*) = 11.0$. With the isolated sample, we measure for the first time the total X-ray luminosity of galaxies with a stellar mass of $(3 \sim 10) \times 10^9 M_\odot$ to be $2.4 \pm 0.9 \times 10^{39}$ erg/s.

3.2. $L_{X,\text{CGM}} - M_*$ relation

We present the CGM luminosity $L_{X,\text{CGM}}$ of the CEN sample as a function of M_* in Fig. 2. Using the models of Paper I, we find that the unresolved AGN and XRBs contribute to about 50% of the L_X for galaxies with $\log(M_*) = 10.0 - 10.5$ and less than $< 20\%$ for more massive galaxies. The hot CGM thus contributes

Table 1: The observed rest-frame X-ray luminosity in the 0.5-2 keV band within R_{500c} in erg s^{-1} of different components for isolated and CEN sample.

$\log_{10}(M_*/M_\odot)$		Isolated sample		CEN sample			
min	max	$L_{X,\text{total}}$ (no mask)	$L_{X,\text{mask}}$ (with mask)	$L_{X,\text{total}}$ (no mask)	$L_{X,\text{mask}}$ (with mask)	$L_{X,\text{CGM}}$	$L_{X,\text{AGN+XRB+SAT}}$ (with mask)
9.5	10.0	$2.4 \pm 0.9 \times 10^{39}$	$4.2 \pm 0.8 \times 10^{39}$	-	-	-	-
10.0	10.5	$1.2 \pm 0.4 \times 10^{40}$	$6.4 \pm 1.4 \times 10^{39}$	$9.5 \pm 4.7 \times 10^{39}$	$4.1 \pm 1.2 \times 10^{39}$	$2.1 \pm 1.3 \times 10^{39}$	$2.0 \pm 0.4 \times 10^{39}$
10.5	11.0	$2.6 \pm 0.7 \times 10^{40}$	$2.2 \pm 0.2 \times 10^{40}$	$3.2 \pm 0.7 \times 10^{40}$	$1.7 \pm 0.2 \times 10^{40}$	$1.2 \pm 0.2 \times 10^{40}$	$5.0 \pm 1.0 \times 10^{39}$
11.0	11.25	$1.2 \pm 0.2 \times 10^{41}$	$8.6 \pm 0.8 \times 10^{40}$	$1.1 \pm 0.2 \times 10^{41}$	$6.8 \pm 0.4 \times 10^{40}$	$5.6 \pm 0.5 \times 10^{40}$	$1.2 \pm 0.2 \times 10^{40}$
11.25	11.5	$4.6 \pm 0.7 \times 10^{41}$	$3.1 \pm 0.3 \times 10^{41}$	$4.1 \pm 0.5 \times 10^{41}$	$2.2 \pm 0.1 \times 10^{41}$	$2.0 \pm 0.1 \times 10^{41}$	$2.4 \pm 0.4 \times 10^{40}$

Notes. At different stellar mass bins (first two columns), the X-ray luminosity of all X-ray emission ($L_{X,\text{total}}$, without masking detected X-ray sources), the X-ray luminosity after excluding detected X-ray sources ($L_{X,\text{mask}}$, with masking X-ray sources), the X-ray luminosity of hot CGM within R_{500c} ($L_{X,\text{CGM}}$), and modeled X-ray luminosity from unresolved AGN, XRB sources and misclassified satellite galaxies ($L_{X,\text{AGN+XRB+SAT}}$).

to about 50 – 80% of the total X-ray luminosity of the central galaxies (after masking detected X-ray sources). The $L_{X,\text{CGM}}$ (purple in Fig. 2, Table 1) increases from $2.1 \pm 1.3 \times 10^{39}$ erg/s to $2.0 \pm 0.4 \times 10^{41}$ erg/s, when $\log(M_*)$ increases from 10.0 to 11.5.

We compare our CGM luminosity to stellar mass relation ($L_{X,\text{CGM}} - M_*$) to the corresponding ones measured by [Anderson et al. \(2015, Fig. 5, bottom panel\)](#). The $L_{X,\text{CGM}}$ in [Anderson et al. \(2015\)](#) is defined as the X-ray emission in $0.15 - 1 \times R_{500}$ (in order to remove the AGN emission). Our $L_{X,\text{CGM}} - M_*$ relation agrees well with [Anderson et al. \(2015\)](#), with smaller uncertainties and significantly improved signal-to-noise measurements for galaxies with $\log(M_*) < 11$.

We fit together all of our measurements and that of [Anderson et al. \(2015\)](#) with a broken power-law (Eq. 3). We get the following best-fit parameters $L_0 = 41.2 \pm 0.1$, $\alpha_1 = 1.9 \pm 0.2$, $\alpha_2 = 4.2 \pm 0.1$, $\log(M_0) = 11.28 \pm 0.03$ and $\delta = 0.05 \pm 0.04$.

We compare the observed $L_{X,\text{CGM}} - M_*$ relation to the ones predicted by simulations: EAGLE, TNG1000, and SIMBA. The simulations may deviate from the observations at some stellar mass range, but given the large scatter, the simulations generally agree with the observations. The reason of higher $L_{X,\text{CGM}}$ predicted by EAGLE for galaxies with $\log(M_*) > 11$ was discussed in [Davies et al. \(2019\)](#).

The baryons follow the gravitational potential well, and the hot CGM luminosity is expected to trace the halo mass ([Tumlinson et al. 2011](#)). Thus, by measuring the relation between CGM luminosity and stellar mass, we probe the Stellar-to-Halo-Mass-Relation (SHMR) in a novel fashion, complementary to probes of SHMR using galaxy clustering and galaxy-galaxy lensing ([Leauthaud et al. 2012b; Velander et al. 2014; Coupon et al. 2015](#)). We discuss the implications of our results further in Sect. 4.3. The broken power-law nature of the relation is new and independent evidence of the different hot feedback processes occurring in different stellar mass ranges.

3.3. $L_{X,\text{total}} - M_{500c}$ and $L_{X,\text{CGM}} - M_{500c}$ relations

This section presents the stack of the CEN_{halo} sample. The $L_{X,\text{total}} - M_{500c}$ relation obtained is plotted in Fig. 3 in green and listed in Table 2. We scale $L_{X,\text{total}}$ by $E(z)^{-2}$ considering a self-similar redshift evolution⁵.

⁵ The self-similar redshift evolution of $E(z)^{-2}$ works for the massive clusters, where the X-ray emission from bremsstrahlung process dominates. For lower mass structures where the line emission dominates, $E(z)^{-5/3}$ is usually taken. Considering the CEN_{halo} sample is below $z = 0.2$ ($E(z) \approx 1.0 - 1.1$) and to keep consistency with clusters studies, we adopt a $E(z)^{-2}$ scaling throughout.

The $L_{X,\text{total}} - M_{500c}$ relation is measured down to $\log(M_{500c}) = 11.3$. The $L_{X,\text{total}}$ increases from $1.4 \pm 0.5 \times 10^{40}$ erg/s at $\log(M_{500c}) = 11.3$ to $1.2 \pm 0.1 \times 10^{42}$ erg/s at $\log(M_{500c}) = 13.7$. The $\log L_{X,\text{total}} - \log M_{500c}$ relation is quasi-linear and can be described with $\log L_{X,\text{total}} = (28.9 \pm 0.5) + (0.96 \pm 0.04) \log M_{500c}$.

The X-ray luminosity of the hot CGM (after modeling of unresolved point sources, Paper I) within R_{500c} ($L_{X,\text{CGM}}$) as a function of M_{500c} is also plotted in Fig. 3 (purple data points) and listed in Table 2. We find that $L_{X,\text{CGM}}$ increases with M_{500c} from $2.7 \pm 0.9 \times 10^{39}$ erg/s at $\log(M_{500c}) = 11.3$ to $9.2 \pm 0.4 \times 10^{41}$ erg/s at $\log(M_{500c}) = 13.7$. The similar uncertainty of $L_{X,\text{CGM}}$ compared to the $L_{X,\text{total}}$ is because that $L_{X,\text{CGM}}$ is derived from the $L_{X,\text{mask}}$ after masking X-ray point sources, where the Jackknife uncertainty is smaller, as we discussed in Sect. 2 and Paper I.

We fit the $L_{X,\text{CGM}} - M_{500c}$ relation with Equation. 2, and get

$$\log(L_{X,\text{CGM}}) = (1.35 \pm 0.04) \log(M_{500c}) + 23.8 \pm 0.5. \quad (4)$$

The $L_{X,\text{CGM}} - M_{500c}$ relation has been extensively studied at the high mass end ([Eckmiller et al. 2011; Lovisari et al. 2015; Mantz et al. 2016; Schellenberger & Reiprich 2017; Adami et al. 2018; Bulbul et al. 2019; Lovisari et al. 2020; Chiu et al. 2022](#)). By stacking the galaxy groups from the GAMA survey, the X-ray emission is detected down to $\log(M_{500c}) = 13.5$ ([Popesso et al. 2023](#)). These previous works are compared to our result in Fig. 3. Our measurement extends the $L_{X,\text{CGM}} - M_{500c}$ relation down to lower mass structure and narrows down the uncertainty by a factor of > 10 for $\log(M_{500c}) < 13.5$ structures.

We compare the $L_{X,\text{CGM}} - M_{500c}$ relations predicted by the simulations to the observed one in Fig. 3. The simulations agree with the observations within 1σ down to $\log(M_{500c}) = 12$, with a slight deviation from SIMBA at lower mass.

4. What do the scaling relations imply?

4.1. Comparing $L_{X,\text{CGM}} - M_{500c}$ to self-similar model

Under the assumption that the gas is heated by gravity only, and the systems (galaxies, galaxy groups, galaxy clusters⁶) reach equilibrium and are isothermal, the properties of the hot gas scale with the dark matter halo mass following the self-similar model ([Lovisari et al. 2021](#)). The deviation of observed relations from

⁶ Following [Lovisari et al. \(2021\)](#), to make the comparison to the scaling relations predicted from the self-similar model easier, in this section, we name the system with $\log(M_{500c}) > 13.4$ as galaxy clusters, $\log(M_{500c}) = 12.8 - 13.4$ as galaxy groups, $\log(M_{500c}) < 12.8$ as galaxies.

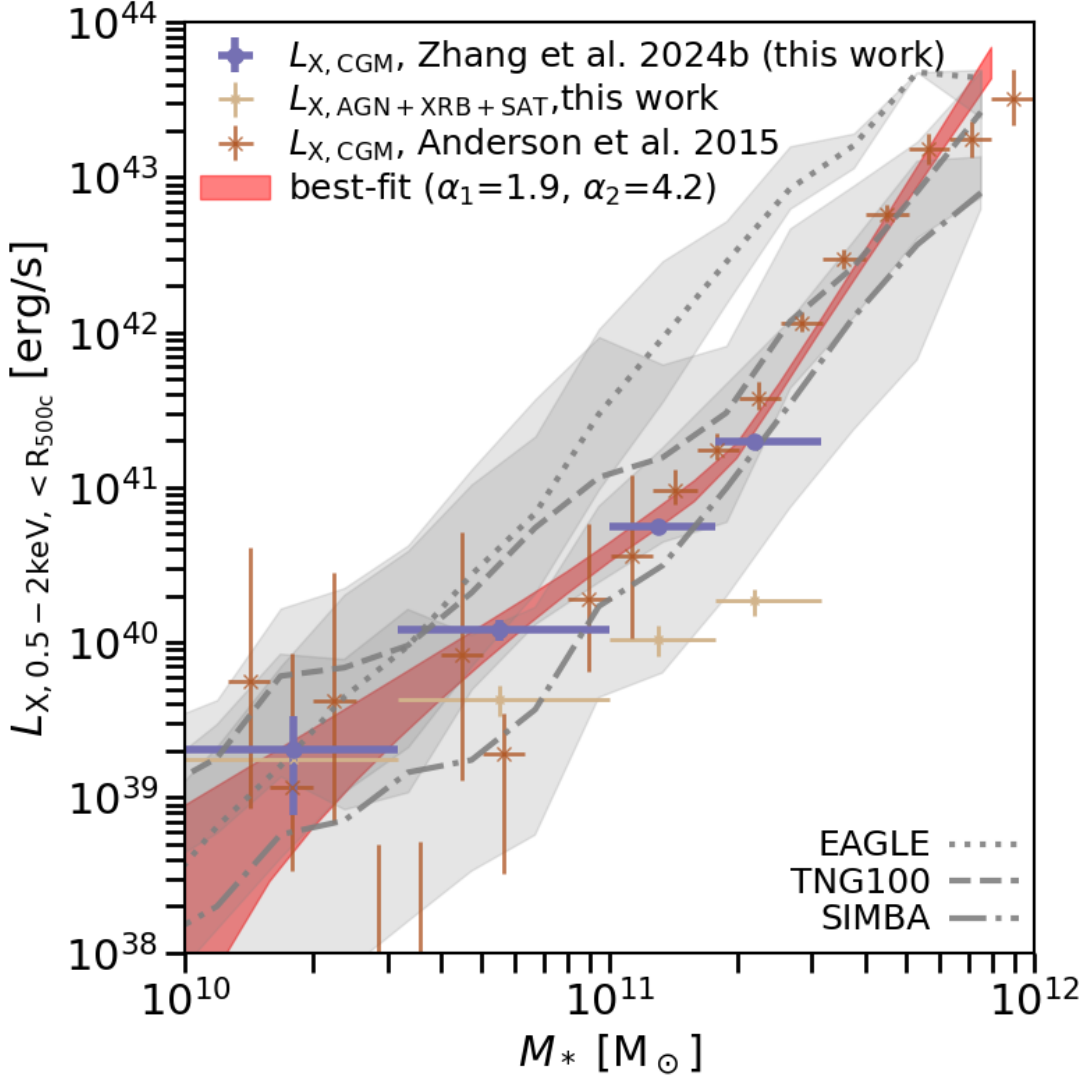


Fig. 2: X-ray luminosity vs. stellar mass. The hot CGM X-ray luminosity ($L_{X,\text{CGM}}$) measured around the CEN sample within R_{500c} in 0.5–2 keV as a function of the M_* is shown in purple. The modeled X-ray luminosity from unresolved AGN, XRB and misclassified satellite ($L_{X,\text{AGN+XRB+SAT}}$) is depicted in tan. The $L_{X,\text{CGM}} - M_*$ measurements from Anderson et al. (2015) are plotted with thin brown crosses. The red band displays the best-fit broken power law model and its 2σ uncertainty. It is adjusted to both sets of observations together. The prediction from the EAGLE, TNG100 and SIMBA simulations compiled following the methodology of Truong et al. (2021) are overlotted in gray with 1σ uncertainties.

the self-similar model implies extra non-gravitational mechanisms must be imported in the gas’s heating, cooling, or ejection.

The self-similar relation of $L_{X,\text{CGM}} - M_{500c}$ of systems with $\log(M_{500c}) > 13.4$ (galaxy clusters) has an index of about 0.78 (solar metallicity gas, $Z = Z_\odot$) to 0.94 ($Z = 0.3Z_\odot$) (Lovisari et al. 2021). The observed slope of the $L_{X,\text{gas}} - M_{500c}$ relation above $\log(M_{500c}) = 14.0$ ranges between 1.5–2.0, steeper than self-similar prediction (Bulbul et al. 2019; Lovisari et al. 2020; Chiu et al. 2022). This has given rise to a widespread discussion of AGN feedback models and their role in heating/modifying the ICM (e.g. Lacey et al. 2016; Pop et al. 2022; Schaye et al. 2023).

For lower-mass systems, the self-similar relation of $L_{X,\text{gas}} - M_{500c}$ is expected to change due to the complexity of the emissivity of the hot plasma as a function of temperature and metallicity in the 0.5-2 keV band (Lovisari et al. 2021). For galaxy groups, the index ranges from 0 ($Z = Z_\odot$) to 0.6 ($Z = 0.3Z_\odot$). However, our observed $L_{X,\text{gas}} - M_{500c}$ has an index of 1.35 ± 0.04 ,

which is much steeper. It strengthens further the need for non-gravitational processes, probably linked to AGN feedback, to explain the properties of the hot CGM at the galaxy group scale (Eckert et al. 2021, Bahar et al., submitted).

For systems with $\log(M_{500c}) < 12.8$ (galaxies), the self-similar model index ranges from 1.5 ($Z = Z_\odot$) to 1.6 ($Z = 0.3Z_\odot$) (Lovisari et al. 2021). We obtain an index of 1.35 ± 0.04 , which is about 15% shallower than self-similar prediction. The two indexes’ closeness might imply that the non-gravitational processes (for example, AGN and stellar feedback) are subdominant in these systems. On the other hand, the CGM around galaxies might not reach equilibrium and virialization, and the self-similar model might not apply; other processes contribute to the observed scaling relation (Faucher-Giguere & Oh 2023).

Table 2: The rest-frame $L_{X,\text{total}}$ in the 0.5-2 keV band in erg s^{-1} of different components for CEN_{halo} sample.

$\log_{10}(M_{200\text{m}}/M_{\odot})$		$\log_{10}(M_{500\text{c}}/M_{\odot})$		CEN _{halo} sample			
min	max	min	max	$L_{X,\text{total}}$ (no mask)	$L_{X,\text{mask}}$ (with mask)	$L_{X,\text{CGM}}$	$L_{X,\text{AGN+XRB+SAT}}$ (with mask)
11.5	12.0	11.3	11.8	$1.4 \pm 0.5 \times 10^{40}$	$5.0 \pm 0.7 \times 10^{39}$	$2.7 \pm 0.9 \times 10^{39}$	$2.3 \pm 0.6 \times 10^{39}$
12.0	12.5	11.8	12.3	$5.7 \pm 0.9 \times 10^{40}$	$1.9 \pm 0.3 \times 10^{40}$	$1.3 \pm 0.3 \times 10^{40}$	$5.9 \pm 1.7 \times 10^{39}$
12.5	13.0	12.3	12.8	$1.1 \pm 0.2 \times 10^{41}$	$5.9 \pm 0.8 \times 10^{40}$	$5.1 \pm 0.8 \times 10^{40}$	$8.5 \pm 1.7 \times 10^{39}$
13.0	13.5	12.8	13.3	$4.3 \pm 1.2 \times 10^{41}$	$2.5 \pm 0.2 \times 10^{41}$	$2.4 \pm 0.2 \times 10^{41}$	$1.5 \pm 0.2 \times 10^{40}$
13.5	14.0	13.3	13.7	$1.2 \pm 0.1 \times 10^{42}$	$9.5 \pm 0.4 \times 10^{41}$	$9.2 \pm 0.4 \times 10^{41}$	$3.3 \pm 0.7 \times 10^{40}$

Notes. The CEN_{halo} sample are binned in $M_{200\text{m}}$ derived based on the group finder algorithm (Tinker 2021), and the corresponding $M_{500\text{c}}$ derived considering the concentration model from Ishiyama et al. (2021). The luminosities are as defined in Table 1.

4.2. Comparison to simulations

The discussion in Sect. 4.1 emphasized that the observed scaling relations contain information about feedback processes. In Fig. 2 and Fig. 3, we compare the observed $L_{X,\text{CGM}} - M_*$ and $L_{X,\text{CGM}} - M_{500\text{c}}$ relations to the EAGLE, TNG100, SIMBA (as compiled by Truong et al. 2021) and FLAMINGO simulations (Braspenning et al. 2023). Although simulations and observations agree within the scatter, there are slight deviations between them.

More detailed comparisons are required to draw quantitative conclusions on the nature of the ejective feedback, the gas enrichment process, and the heating mechanism. In this work, we do not create a dedicated mock catalog mimicking possible selection effects, which could be improved in future works. If a simulation can reproduce both relations between halo mass and the CGM or the total (adding AGN and XRB) luminosity, it would constitute good evidence for the feedback mechanisms to be accurate. This, however, also requires accurate prediction of the X-ray emission from AGN and XRB (e.g. Biffi et al. 2018; Vladutescu-Zopp et al. 2023)

4.3. A broken power law $L_{X,\text{CGM}} - M_*$ relation

We detected a broken power law relation $L_{X,\text{CGM}} - M_*$ (see Fig. 2) and a single power law relation $L_{X,\text{CGM}} - M_{500\text{c}}$ (see Fig. 3). The SHMR of the CEN galaxy sample used by Tinker (2021) is well represented by the broken power law

$$M_* = 0.1 M_{200\text{m}} \left[\left(\frac{M_{200\text{m}}}{5 \times 10^{11}} \right)^{-0.98} + \left(\frac{M_{200\text{m}}}{5 \times 10^{11}} \right)^{0.63} \right]^{-1}, \quad (5)$$

with a scatter of 0.15 dex. We then convolve the SHMR to $L_{X,\text{CGM}} - M_{500\text{c}}$ to predict the relation between $L_{X,\text{CGM}}$ and M_* . In Fig. 4, we show both the observed and predicted (from SHMR and $L_{X,\text{CGM}} - M_{500\text{c}}$) $L_{X,\text{CGM}} - M_*$ relations. The agreement of the two indeed demonstrates that the measured hot X-ray (CGM) luminosity is a good tracer of the gravitation potential of the halos. This brings the possibility of a new method to measure the SHMR relation by jointly fitting the relations $L_{X,\text{CGM}} - M_*$ and $L_{X,\text{CGM}} - M_{500\text{c}}$.

5. Summary and conclusions

In this work, we extend our view of the scaling relations between X-ray emission from the hot circum-galactic medium and galaxies' main properties (stellar and halo mass). These scaling relations can be used to constrain galaxy evolution models.

Following the analysis presented in Paper I, we use the integrated quantities (total luminosities within a fixed aperture of $R_{500\text{c}}$) directly measured from stacking eRASS:4 X-ray photons around galaxies in well-defined, highly complete samples built from the SDSS and LS DR9 galaxy catalogs containing 85222 central galaxies split into stellar mass bins, 125512 central galaxies split in halo mass bins, and 213514 isolated galaxies. We report the following three findings, which constitute a new benchmark to constrain galaxy formation and evolution models:

1. The scaling relation between the X-ray luminosity $L_{X,\text{total}}$ (total X-ray emission within $R_{500\text{c}}$) and stellar mass of galaxies ($L_{X,\text{total}} - M_*$) is measured for galaxies with $\log(M_*) > 9.5$ thanks to the large photometric isolated galaxy sample (Fig. 1).
2. The scaling relation between the X-ray luminosity of hot CGM and stellar mass ($L_{X,\text{CGM}} - M_*$) is measured for central galaxies with $\log(M_*) > 10.0$ (Fig. 2). A double power law describes the $L_{X,\text{CGM}} - M_*$ relation, with the break at $\log(M_*) = 11.28$, power-law indices of ≈ 1.9 (≈ 4.2) below (above) the break.
3. The scaling relations between X-ray luminosity and halo mass of galaxies ($L_{X,\text{total}} - M_{500\text{c}}$), X-ray luminosity of hot CGM and halo mass ($L_{X,\text{CGM}} - M_{500\text{c}}$) are measured down to $M_{500\text{c}} = 11.3$ (Fig. 3). In this mass range, the $L_{X,\text{CGM}} - M_{500\text{c}}$ relation can be described by a single power law with index ≈ 1.35 .

In the future, with deeper spectroscopic galaxy surveys, i.e. DESI BGS and 4MOST (Zarrouk et al. 2022; Hahn et al. 2023; de Jong et al. 2019; Finoguenov et al. 2019), we will enlarge the spectroscopic galaxy sample to cover wider areas (3-4 times that used here) and extend further in redshift (up to $z < 0.4$). We expect an apparent increase in signal-to-noise and to obtain a detailed view of the hot CGM and possible relation to intermediate-mass black holes in and around dwarf galaxies ($\log(M_*) < 10$) (Arcodia et al. 2023).

Acknowledgements. This project acknowledges financial support from the European Research Council (ERC) under the European Union's Horizon 2020 research and innovation program HotMilk (grant agreement No. 865637). GP acknowledges support from Bando per il Finanziamento della Ricerca Fondamentale 2022 dell'Istituto Nazionale di Astrofisica (INAF): GO Large program and from the Framework per l'Attrazione e il Rafforzamento delle Eccellenze (FARE) per la ricerca in Italia (R20L5S39T9). NT acknowledges support from NASA under award number 80GSFC21M0002.

This work is based on data from eROSITA, the soft X-ray instrument aboard SRG, a joint Russian-German science mission supported by the Russian Space Agency (Roskosmos), in the interests of the Russian Academy of Sciences represented by its Space Research Institute (IKI), and the Deutsches Zentrum für Luft- und Raumfahrt (DLR). The SRG spacecraft was built by Lavochkin Association (NPOL) and its subcontractors, and is operated by NPOL with support from the Max Planck Institute for Extraterrestrial Physics (MPE).

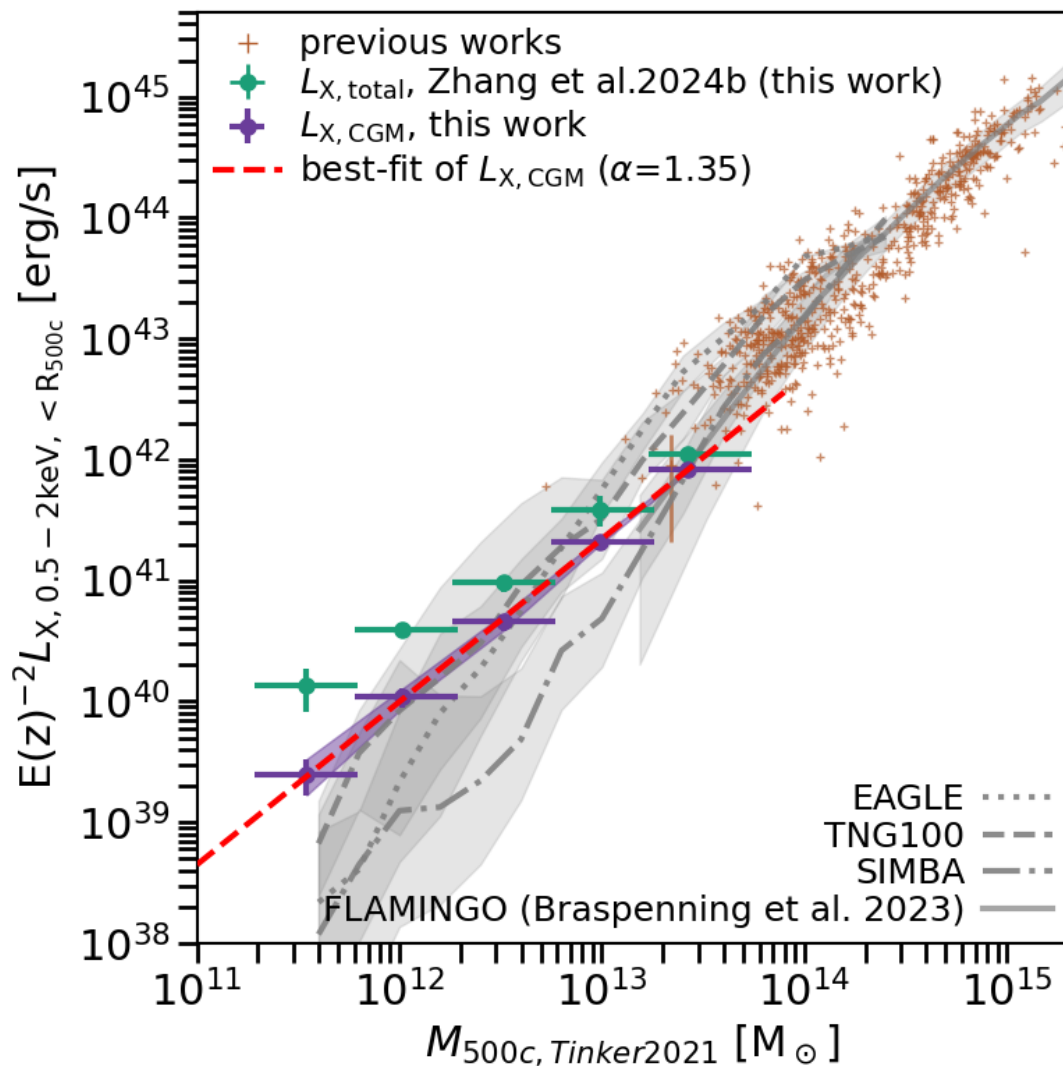


Fig. 3: The total X-ray luminosity ($L_{X,\text{total}}$, green) and X-ray luminosity of hot gas ($L_{X,\text{CGM}}$, purple) within R_{500c} in 0.5 – 2 keV as a function of the M_{500c} . The red dashed line is the best-fit single power law to our measurements (purple) of the $L_{X,\text{CGM}} - M_{500c}$ relation. The brown data points are taken from Eckmiller et al. (2011); Lovisari et al. (2015); Mantz et al. (2016); Schellenberger & Reiprich (2017); Adami et al. (2018); Bulbul et al. (2019); Lovisari et al. (2020); Liu et al. (2022); Popesso et al. (2023) (Notice the presence of selection effects and Malmquist bias in these observations). The $L_{X,\text{CGM}} - M_{500c}$ relations predicted by simulations EAGLE, TNG100, SIMBA and FLAMINGO with 1σ uncertainties are overplotted in gray (Truong et al. 2020; Comparat et al. 2022; Braspenning et al. 2023).

The development and construction of the eROSITA X-ray instrument was led by MPE, with contributions from the Dr. Karl Remeis Observatory Bamberg & ECAP (FAU Erlangen-Nuernberg), the University of Hamburg Observatory, the Leibniz Institute for Astrophysics Potsdam (AIP), and the Institute for Astronomy and Astrophysics of the University of Tübingen, with the support of DLR and the Max Planck Society. The Argelander Institute for Astronomy of the University of Bonn and the Ludwig Maximilians Universität Munich also participated in the science preparation for eROSITA.

The eROSITA data shown here were processed using the eSASS/NRTA software system developed by the German eROSITA consortium.

Funding for the SDSS and SDSS-II has been provided by the Alfred P. Sloan Foundation, the Participating Institutions, the National Science Foundation, the U.S. Department of Energy, the National Aeronautics and Space Administration, the Japanese Monbukagakusho, the Max Planck Society, and the Higher Education Funding Council for England. The SDSS Web Site is <http://www.sdss.org/>. The SDSS is managed by the Astrophysical Research Consortium for the Participating Institutions. The Participating Institutions are the American Museum of Natural History, Astrophysical Institute Potsdam, University of Basel, University of Cambridge, Case Western Reserve University, University of Chicago, Drexel University, Fermilab, the Institute for Advanced

Study, the Japan Participation Group, Johns Hopkins University, the Joint Institute for Nuclear Astrophysics, the Kavli Institute for Particle Astrophysics and Cosmology, the Korean Scientist Group, the Chinese Academy of Sciences (LAMOST), Los Alamos National Laboratory, the Max-Planck-Institute for Astronomy (MPIA), the Max-Planck-Institute for Astrophysics (MPA), New Mexico State University, Ohio State University, University of Pittsburgh, University of Portsmouth, Princeton University, the United States Naval Observatory, and the University of Washington.

The DESI Legacy Imaging Surveys consist of three individual and complementary projects: the Dark Energy Camera Legacy Survey (DECaLS), the Beijing-Arizona Sky Survey (BASS), and the Mayall z-band Legacy Survey (MzLS). DECaLS, BASS and MzLS together include data obtained, respectively, at the Blanco telescope, Cerro Tololo Inter-American Observatory, NSF’s NOIRLab; the Bok telescope, Steward Observatory, University of Arizona; and the Mayall telescope, Kitt Peak National Observatory, NOIRLab. NOIRLab is operated by the Association of Universities for Research in Astronomy (AURA) under a cooperative agreement with the National Science Foundation. Pipeline processing and analyses of the data were supported by NOIRLab and the Lawrence Berkeley National Laboratory (LBNL). Legacy Surveys also uses data products from the Near-Earth Object Wide-field Infrared Survey Explorer

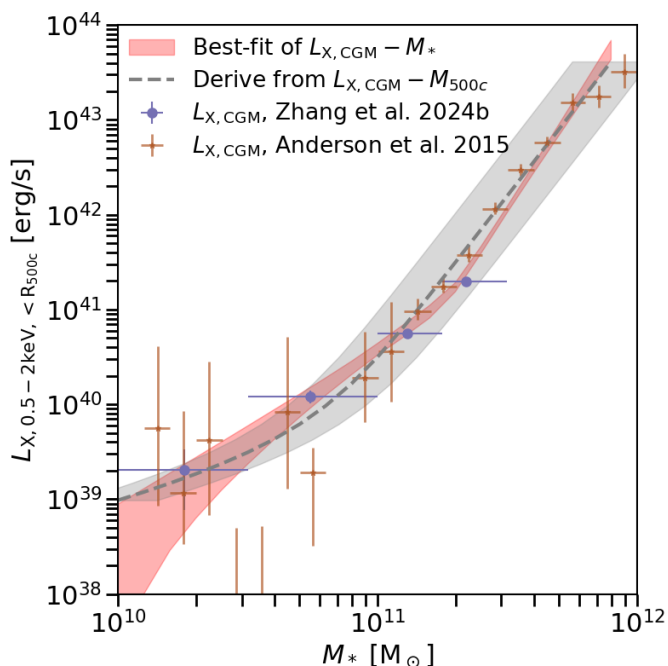


Fig. 4: The observed X-ray luminosity of CGM within R_{500c} in 0.5 – 2 keV as a function to M_* (purple, brown points) and the best fit (red band), compared to the relation derived from SHMR (gray band).

(NEOWISE), a project of the Jet Propulsion Laboratory/California Institute of Technology, funded by the National Aeronautics and Space Administration. Legacy Surveys was supported by: the Director, Office of Science, Office of High Energy Physics of the U.S. Department of Energy; the National Energy Research Scientific Computing Center, a DOE Office of Science User Facility; the U.S. National Science Foundation, Division of Astronomical Sciences; the National Astronomical Observatories of China, the Chinese Academy of Sciences and the Chinese National Natural Science Foundation. LBNL is managed by the Regents of the University of California under contract to the U.S. Department of Energy. The complete acknowledgments can be found at <https://www.legacysurvey.org/acknowledgment/>.

The Siena Galaxy Atlas was made possible by funding support from the U.S. Department of Energy, Office of Science, Office of High Energy Physics under Award Number DE-SC0020086 and from the National Science Foundation under grant AST-1616414.

References

- Adami, C., Giles, P., Koulouridis, E., et al. 2018, *A&A*, 620, A5
 Anderson, M. E., Gaspari, M., White, S. D. M., Wang, W., & Dai, X. 2015, *MNRAS*, 449, 3806
 Andrae, R. 2010, arXiv e-prints, arXiv:1009.2755
 Arcodia, R., Merloni, A., Comparat, J., et al. 2023, arXiv e-prints, arXiv:2311.16220
 Biffi, V., Dolag, K., & Merloni, A. 2018, *MNRAS*, 481, 2213
 Bilicki, M., Peacock, J. A., Jarrett, T. H., et al. 2016, *ApJS*, 225, 5
 Braspenning, J., Schaye, J., Schaller, M., et al. 2023, arXiv e-prints, arXiv:2312.08277
 Bulbul, E., Chiu, I. N., Mohr, J. J., et al. 2019, *ApJ*, 871, 50
 Chadayammuri, U., Bogdán, Á., Oppenheimer, B. D., et al. 2022, *ApJ*, 936, L15
 Chiu, I. N., Ghirardini, V., Liu, A., et al. 2022, *A&A*, 661, A11
 Choi, E., Ostriker, J. P., Naab, T., Oser, L., & Moster, B. P. 2015, *MNRAS*, 449, 4105
 Comparat, J., Truong, N., Merloni, A., et al. 2022, *A&A*, 666, A156
 Coupon, J., Arnouts, S., van Waerbeke, L., et al. 2015, *MNRAS*, 449, 1352
 Crain, R. A., Schaye, J., Bower, R. G., et al. 2015, *MNRAS*, 450, 1937
 Das, S., Chiang, Y.-K., & Mathur, S. 2023, *ApJ*, 951, 125
 Davé, R., Anglés-Alcázar, D., Narayanan, D., et al. 2019, *MNRAS*, 486, 2827
 Davies, J. J., Crain, R. A., McCarthy, I. G., et al. 2019, *MNRAS*, 485, 3783

- de Jong, R. S., Agertz, O., Berbel, A. A., et al. 2019, *The Messenger*, 175, 3
 Dey, A., Schlegel, D. J., Lang, D., et al. 2019, *AJ*, 157, 168
 Eckert, D., Gaspari, M., Gastaldello, F., Le Brun, A. M. C., & O’Sullivan, E. 2021, *Universe*, 7, 142
 Eckmiller, H. J., Hudson, D. S., & Reiprich, T. H. 2011, *A&A*, 535, A105
 Faucher-Giguere, C.-A. & Oh, S. P. 2023, arXiv e-prints, arXiv:2301.10253
 Finoguenov, A., Merloni, A., Comparat, J., et al. 2019, *The Messenger*, 175, 39
 Forbes, D. A., Alabi, A., Romanowsky, A. J., et al. 2017, *MNRAS*, 464, L26
 Goulding, A. D., Greene, J. E., Ma, C.-P., et al. 2016, *ApJ*, 826, 167
 Hahn, C., Wilson, M. J., Ruiz-Macias, O., et al. 2023, *AJ*, 165, 253
 Hogg, D. W., Bovy, J., & Lang, D. 2010, arXiv e-prints, arXiv:1008.4686
 Ishiyama, T., Prada, F., Klypin, A. A., et al. 2021, *MNRAS*, 506, 4210
 Iyer, K., Gawiser, E., Davé, R., et al. 2018, *ApJ*, 866, 120
 Kim, D.-W. & Fabbiano, G. 2013, *ApJ*, 776, 116
 Kim, D.-W. & Fabbiano, G. 2015, *ApJ*, 812, 127
 Lacey, C. G., Baugh, C. M., Frenk, C. S., et al. 2016, *MNRAS*, 462, 3854
 Leauthaud, A., George, M. R., Behroozi, P. S., et al. 2012a, *ApJ*, 746, 95
 Leauthaud, A., Tinker, J., Bundy, K., et al. 2012b, *ApJ*, 744, 159
 Li, J.-T. & Wang, Q. D. 2013, *MNRAS*, 435, 3071
 Liu, A., Bulbul, E., Ghirardini, V., et al. 2022, *A&A*, 661, A2
 Lovisari, L., Ettori, S., Gaspari, M., & Giles, P. A. 2021, *Universe*, 7, 139
 Lovisari, L., Reiprich, T. H., & Schellenberger, G. 2015, *A&A*, 573, A118
 Lovisari, L., Schellenberger, G., Sereno, M., et al. 2020, *ApJ*, 892, 102
 Mantz, A. B., Allen, S. W., Morris, R. G., & Schmidt, R. W. 2016, *MNRAS*, 456, 4020
 Marinacci, F., Vogelsberger, M., Pakmor, R., et al. 2018, *MNRAS*, 480, 5113
 McAlpine, S., Helly, J. C., Schaller, M., et al. 2016, *Astronomy and Computing*, 15, 72
 McIntosh, A. 2016, arXiv e-prints, arXiv:1606.00497
 Merloni, A., Lamer, G., Liu, T., et al. 2024, *A&A*, 682, A78
 Merloni, A., Predehl, P., Becker, W., et al. 2012, arXiv e-prints, arXiv:1209.3114
 Mowla, L., van der Wel, A., van Dokkum, P., & Müller, T. B. 2019a, *ApJ*, 872, L13
 Mowla, L. A., van Dokkum, P., Brammer, G. B., et al. 2019b, *ApJ*, 880, 57
 Muldrew, S. I., Croton, D. J., Skibba, R. A., et al. 2012, *MNRAS*, 419, 2670
 Naiman, J. P., Pillepich, A., Springel, V., et al. 2018, *MNRAS*, 477, 1206
 Nelson, D., Pillepich, A., Springel, V., et al. 2019a, *MNRAS*, 490, 3234
 Nelson, D., Springel, V., Pillepich, A., et al. 2019b, *Computational Astrophysics and Cosmology*, 6, 2
 Pandey, S., Gatti, M., Baxter, E., et al. 2022, *Phys. Rev. D*, 105, 123526
 Pillepich, A., Nelson, D., Hernquist, L., et al. 2018, *MNRAS*, 475, 648
 Planck Collaboration, Ade, P. A. R., Aghanim, N., et al. 2013, *A&A*, 557, A52
 Planck Collaboration, Aghanim, N., Akrami, Y., et al. 2020, *A&A*, 641, A6
 Pop, A.-R., Hernquist, L., Nagai, D., et al. 2022, arXiv e-prints, arXiv:2205.11528
 Popesso, P., Biviano, A., Bulbul, E., et al. 2023, *MNRAS*[arXiv:2302.08405]
 Predehl, P., Andritschke, R., Arefiev, V., et al. 2021, *A&A*, 647, A1
 Schaan, E., Ferraro, S., Amodeo, S., et al. 2021, *Phys. Rev. D*, 103, 063513
 Schaller, M., Dalla Vecchia, C., Schaye, J., et al. 2015, *MNRAS*, 454, 2277
 Schaye, J., Crain, R. A., Bower, R. G., et al. 2015, *MNRAS*, 446, 521
 Schaye, J., Kugel, R., Schaller, M., et al. 2023, *MNRAS*, 526, 4978
 Schellenberger, G. & Reiprich, T. H. 2017, *MNRAS*, 469, 3738
 Smith, R. K., Brickhouse, N. S., Liedahl, D. A., & Raymond, J. C. 2001, *ApJ*, 556, L91
 Springel, V., Pakmor, R., Pillepich, A., et al. 2018, *MNRAS*, 475, 676
 Strauss, M. A., Weinberg, D. H., Lupton, R. H., et al. 2002, *AJ*, 124, 1810
 Sunyaev, R., Arefiev, V., Babyshkin, V., et al. 2021, *A&A*, 656, A132
 Tinker, J. L. 2021, *ApJ*, 923, 154
 Tinker, J. L. 2022, *AJ*, 163, 126
 Truong, N., Pillepich, A., Nelson, D., et al. 2023, *MNRAS*, 525, 1976
 Truong, N., Pillepich, A., Nelson, D., Werner, N., & Hernquist, L. 2021, *MNRAS*, 508, 1563
 Truong, N., Pillepich, A., Werner, N., et al. 2020, *MNRAS*, 494, 549
 Tumlinson, J., Thom, C., Werk, J. K., et al. 2011, *Science*, 334, 948
 Velander, M., van Uitert, E., Hoekstra, H., et al. 2014, *MNRAS*, 437, 2111
 Vladutescu-Zopp, S., Biffi, V., & Dolag, K. 2023, *A&A*, 669, A34
 Wang, Q. D., Li, J., Jiang, X., & Fang, T. 2016, *MNRAS*, 457, 1385
 Whitaker, K. E., van Dokkum, P. G., Brammer, G., & Franx, M. 2012, *ApJ*, 754, L29
 White, S. D. M. & Rees, M. J. 1978, *MNRAS*, 183, 341
 Zarrouk, P., Ruiz-Macias, O., Cole, S., et al. 2022, *MNRAS*, 509, 1478
 Zou, H., Gao, J., Zhou, X., & Kong, X. 2019, *ApJS*, 242, 8